Understanding the Role of Solution Equilibrium and Precipitation Rate on Precursor Composition for Lithium-ion Battery Active Materials

Hongxu Dong

December 2016

Table of Contents

Acknowledgements

I would like to thank my advisor Professor Gary Koenig for his mentorship. I am very grateful to have met such a helpful and nice advisor, who always respects my thoughts and always loves to share all the knowledge and resources he has. I'd also like to thank my fellow Koenig lab group members James Pierce Robinson, Ethan Paharik, Colin Qi, Charles Michaelis, and Devanshi Gupta for their friendship and assistance in the lab, and my boyfriend Gilbert Liu for his companionship. I would also like to thank Professor Gaurav Giri and Professor Sen Zhang for serving on my M.S. Committee.

Abstract

Transition metal oxides are among the most successful lithium-ion battery cathode materials. Much prior work has been completed in the literature describing the sensitivity of final electrochemical performance of the active materials to the detailed composition and processing of the transition metal oxides. Co-precipitation is a popular, scalable route to synthesize these transition metal oxide cathode materials. First, a precursor is synthesized through co-precipitation using solution chemistry, followed by mixing the precursor particles with a lithium salt and calcining the mixture at elevated temperature to produce the final desired material. The particle morphology of the precursor can be well-retained even after high temperature firing, which makes this synthesis approach an attractive method to achieve control over particle size and shape; however, the deviation of the precursor composition from feed conditions is a challenge that has generally been ignored in previous studies. Using a target final material of the high voltage spinel $LiMn_{1.5}Ni_{0.5}O_4$ as an example, we show in this study that the compositional deviation caused by the co-precipitation reaction to form the precursor particles can play an important role in determining the electrochemical properties of the final active materials. A series of studies were conducted to understand the role of solution equilibrium and rate of precipitation of the transition metals during precursor formation. This knowledge was then used to provide rational control of the precursor composition and finally to synthesize, with high precision, the target stoichiometry necessary to produce $LiMn_{1.5}Ni_{0.5}O_4$.

Introduction

Due to their high energy density, lithium-ion batteries have become a popular choice for applications ranging in scale from consumer electronics to electric vehicles and stationary energy storage systems. Especially with regards to cathode materials, lithium-ion batteries do not have a single material structure or composition that dominates but have many different materials that may be suited to a particular performance or cost objective[1–34]. Many current and future commercial cathode materials are multicomponent transition metal oxides including $LiNiCoAlO_2$[17–21], $LiNi_{1/3}Mn_{1/3}Co_{1/3}O_2$[13–16], $LiNi_{0.5}Mn_{0.5}O_2$, $LiMn_{1.5}Ni_{0.5}O_4$[22–33,35], and $(x)LiMn_2O_3(1-x)LiNMC$. Many of these materials have been reported to have material structure and electrochemical performance that is highly sensitive to the stoichiometry of the final material.

Various routes have also been reported in the literature to synthesize multicomponent metal oxide cathode materials, including direct conversion of individual precursors using solid-state routes[36–42], hydrothermal synthesis[43–46], spray pyrolysis[47–51], and various deposition techniques[52–55]. One method that is very popular in the literature is co-precipitation of precursors followed by calcination to final active. Co-precipitation has the advantages that it is relatively easy to perform in the lab, is scalable, allows tunable and monodisperse particle morphologies[18,56–80] and provides homogeneous mixing of the multiple transition metal components throughout the secondary particles. While co-precipitation has many advantages and there are many reports in the battery literature synthesizing high performance materials using this method, one common assumption of materials produced via co-precipitation is that the particles retain the stoichiometry of the feed solution. However, depending on solution conditions this may not be a reasonable assumption. Van Bommel et al. previously showed through equilibrium calculations

that the fraction of Ni, Mn, and Co during hydroxide co-precipitation with a chelating agent that remains in solution during co-precipitation is highly variable and pH dependent[81]. While this study suggests that predictive calculations should be done to adjust the feed stoichiometry to target the desired precipitate stoichiometry, this is rarely reported. Of the 150 co-precipitation papers cited from the recent literature above, only 6 performed equilibrium calculations as part of their analysis[68,81–85], none used this analysis to guide their feed conditions, only some confirmed the stoichiometry of the transition metals in the precipitate[68,71,73,74,86–89,89–95], and none considered whether the relative rate of co-precipitation was different for the different transition metals. In this paper, we will use equilibrium calculations to guide the selection of feed conditions to achieve precursors with explicit composition control and will demonstrate the importance of such control for some solution conditions and impact on the electrochemical behavior of an exemplar cathode material. We will also demonstrate measurements extent of co-precipitation of each transition metal independently in solution and discuss the potential importance of such analysis.

For this study, we will demonstrate our methods for the target cathode material $LiMn_{1.5}Ni_{0.5}O_4$, and to produce the material will synthesize a target $Mn_{0.75}Ni_{0.25}C_2O_4 \cdot 2H_2O$ precursor, or 3:1 target Mn:Ni ratio. We have chosen the oxalate co-precipitation chemistry because in isolation both Mn and Ni form oxalate dehydrate precipitates in aqueous solution exposed to air. Carbonate co-precipitation is another popular method to synthesize 3:1 Mn:Ni; however NiCO3 is difficult to form as a stable precipitate[84,85,96–100]. Hydroxide co-precipitation is also more complex because of the tendency of Mn to oxidize to $MnOOH$[76,81,86,92,95,101,102]. The oxalate co-precipitation chemistry forms stable precipitates across a range of Mn:Ni ratios and is also compatible with other transition metals such as cobalt[59,70,75,76,79]. Most of the hydroxide and

carbonate co-precipitations are at very high concentration where the stoichiometry deviation from the feed ratio due to the residual TM ions in the solution may become diminished; however, the morphology control studies are often at low concentration and with chelation or structure directing agents where equilibrium and rate of precipitation need to be more carefully considered and predefined. In this paper will use equilibrium calculations to predetermine feed stoichiometry, not just stoichiometry of feed stoichiometry which can lead to significant deviations in final material; also demonstrate that rate of precipitation of transition metals needs to be considered, though the formation of seeds likely mitigates this effect under some conditions. Oxalate is less popular for translation to industry due to low tap density, especially after firing, but our analysis will be translatable to hydroxide and carbonate as well.

2. Background

2.1. LNMO Structure and the Importance of Correct Stoichiometry of LNMO

Since Admine et al. proposed spinel $LiNi_{0.5}Mn_{1.5}O_4$ (LNMO) as a promising cathode material in 1996, intensive investigations have been made about this material because of its high energy (~658 Wh kg^{-1}) and power capabilities, and fast three-dimensional lithium-ion diffusion in the spinel lattices [33,34,80,103–112]. The most remarkable property of LNMO is its discharge voltage plateau at 4.7 V, compared to the 4 V working voltage of most cathode materials represented primarily by layered $LiCoO_2$, spinel $LiMn_2O_4$ and olivine $LiFePO_4$. Such high voltage enables spinel LNMO to provide high energy output and makes it a good candidate for transportation and energy storage applications. Another important advantage of high voltage spinel is the three dimensional network of Li ion diffusion path, as compared to the two-dimensional layered structures and one-dimensional olivine structures. Three dimensional diffusion pathway indicates less diffusion impedance and thus higher Li ion diffusion rate, which is beneficial for cell charge and discharge at high rate. However, the electrochemical properties of LNMO are found to be strongly dependent on particle size and morphology, crystallinity, degree of disorder and impurities, stoichiometry, etc., making the correlation among synthesis, structure, and performance a great challenge[104,106,111,113–119]. Therefore, major advances in preparation technology and property control are highly required to further improve the electrochemical performances of LNMO.

The nominal spinel LNMO is cubic with Li on the tetrahedral sites of the structure. Depending on the distribution of Mn and Ni ions in the lattice, LNMO has two different crystallographic structure: with disordered Ni and Mn on the octahedral sites, the cubic spinels have the space

group Fd3m (as shown in Figure 1 (a), nickel ions distribute in the same sites as manganese ions), and the ordering of Ni^{2+} and Mn^{4+} in LNMO gives the space group $P4_332$ (Figure 1 (b)). In synthesizing spinel LNMO the high calcination temperature leads to the oxygen loss, followed by the reduction of manganese from Mn^{4+} to Mn^{3+}, which results in the Fd3m disordered structure [118]. Annealing at 700°C after the high temperature calcination (850°C or higher) reoxidizes the manganese ion back to 4+ state and transformed the spinel to primitive cubic ordered structure [33,120]. Whether the ordered or disordered LNMO is favored for improving the electrochemical performance remains a subject of debate. The electron hopping from residual Mn^{3+} to Mn^{4+} is confirmed to enhance the electronic conductivity of the disordered spinel [121]; however, the reduce of Mn^{3+} content also enhance the stability of the cell since Mn^{3+} is known to undergo a disproportionation reaction,

$$2Mn^{3+} = Mn^{2+} + Mn^{4+}$$

and Mn^{2+} tends to dissolve into the electrolyte and migrate to the anode to degrade the cells. Therefore it may exist an optimum concentration of Mn^{3+} that trades off between chemical stability and electrochemical performance.
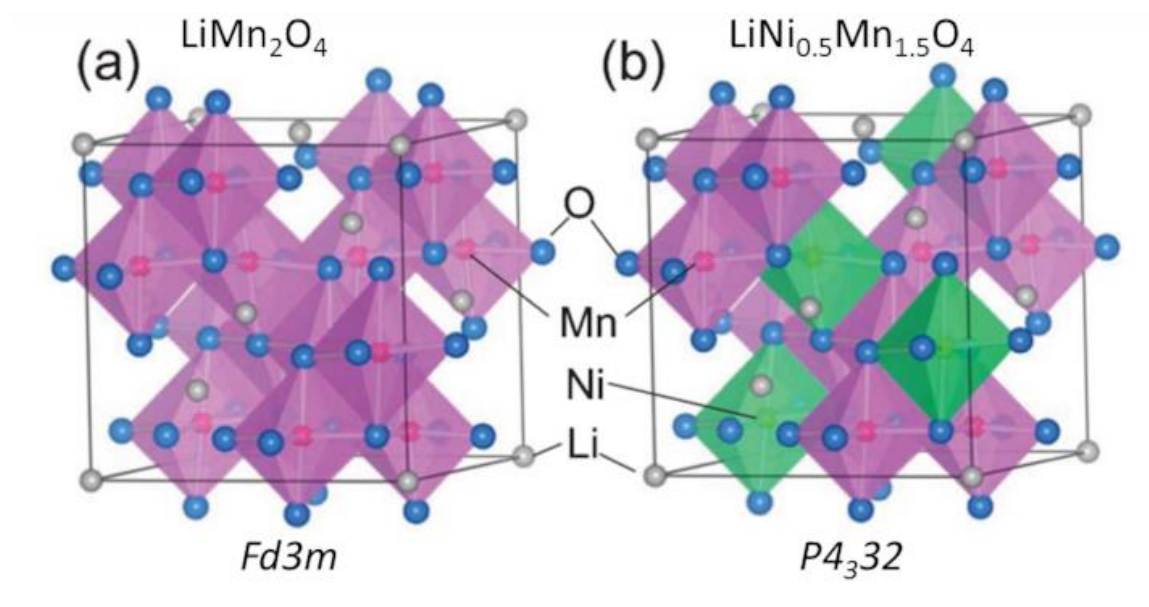
Figure 1 The crystal structure of (a) disordered LNMO (Fd3m phase) and (b) ordered LNMO (P4$_3$32 phase).

Getting the chemical composition right is essential for extracting the capacity as close to the theoretical value. For the ideal LMNO spinel materials, the molecular ratio of Mn/Ni is 3/1, where theoretically all the capacity comes from the Ni^{2+}/Ni^{4+} redox couple. When there is Mn/Ni deviation from the ideal case, however, either Mn rich condition or Ni rich condition may cause different changes in both the oxidation status and the crystal phase, thus influencing the electrochemical performances. Since Ni in $LiNi_{0.5}Mn_{1.5}O_4$ is at 2+ status, we can reasonably assume that nickel ions in the whole series of Mn rich $LiNi_xMn_{2-x}O_4$ materials with $0<x<0.5$ are also Ni^{2+}, which is the lowest possible oxidation status of Ni ion. Taking the charge neutrality into account, we are able to calculate the Mn^{3+} and Mn^{4+} content in the materials, written the formula as $LiNi_x^{2+}Mn_{1-2x}^{3+}Mn_{1+x}^{4+}O_4$. Also assuming that the 4.7 V high voltage capacity comes from the nickel redox couple, and that Mn^{3+}/Mn^{4+} redox couple gives the ~4.1 V plateau during

cycling, we expect to get 2x Li capacity per formula unit at ~4.7V and (1-2x) Li capacity at ~4.1V, which have been observed experimentally[5,59,122–124]. Within this Mn rich range, the materials stays stable in the spinel phase, $LiMn_2O_4$ being the extreme case. More Mn content results in more fraction of Mn^{3+} ions which potentially results in Jahn-Teller distortion and is detrimental to the structure stabilization; therefore a shorter cycle life is expected, compared to the stoichiometry correct LNMO. Going to the other direction of deviation, we have 0.5<x<1 for the nickel rich condition. Since the Mn^{4+} cannot be further oxidized, the oxidation status of nickel ions are partially raised from 2+ to 3+ to meet charge neutralily; doing similar calculation as above, the formula can be written as $LiNi^{2+}_{1-x}Ni^{3+}_{2x-1}Mn^{4+}_{2-x}O_4$. Summing up the Ni^{2+}/Ni^{4+} and the Ni3+/Ni4+ couples, which both contribute to the 4.7 V high voltage capacity, we realize that the high voltage capacity keeps constant in the whole range, $LiNi^{3+}Mn^{4+}O_4$ being the extreme case. Based on the analysis above, if the deviation goes into the Ni rich direction, there seems to be no sacrifice of high voltage capacity. However as there is more Ni in the structure, the risk of forming a rock-salt impurity phase significantly increases which deteriorate both the electron and ion conductivity; thus the rate capability is predicted to be poor compared with the stoichiometric correct LNMO. The phase impurity related structural instability is also another problem for the Ni rich materials. As the end point materials, $LiNi^{3+}Mn^{4+}O_4$ is detected to be more of a rock-salt layered structure, showing similar XRD pattern to $LiNiO_2$ materials. This means that there may exist a phase transition in this range from spinel to layered structure, or a mixture of both two phases exist within this whole range. Whatever the case is, the layered phase structure has a severe risk of phase segregation for Mn content, since Li-Mn-O cannot stay stable in a layered structure[5,59,122–124]. Such phase segregation may cause the electrode degradation and render the cycle life much shorter.

2.2. Oxalate Co-Precipitation in Li-ion Battery Cathode Material Synthesis

Transition metal oxide cathode materials are generally synthesized through either solid-state methods or wet chemical synthesis. In the solid-state synthetic process, appropriate amounts of lithium, manganese, and nickel compounds are mixed and heated up to high temperature which renders the whole process simple and easy for mass production, but this also has the disadvantage of impurity contamination and thus worse electrochemical performance. In comparison, the wet chemical methods allow for molecular level control of the material, and are also relatively less energy consuming since it requires relatively low calcination temperature. Among the wet chemical methods, co-precipitation reactions based on hydroxide and carbonate precipitation have been widely used for chemically homogeneous precursors [81,125–129]. The main advantages of co-precipitation methods include low cost of the raw materials (usually transition metal sulfate), wide solid solution range of mixed transition metal precipitates, and precise control over particle morphology and size; however some major difficulties in the synthesis procedure are often encountered and still not addressed. For instance, in the hydroxide precipitation Mn^{2+} is easily oxidized into Mn^{3+} and further into Mn^{4+} by oxygen under alkaline condition, which causes the Mn/Ni ratio deviate from the ideal value; and in the case of carbonate precipitation, the continuous secondary particle growth makes the particle size and morphology hard to control, and the large surface area also renders the powder vulnerable to moisture in air and make it hard to calcine with the right amount of lithium salts. As a consequence, the oxalate precipitation is being considered an alternative process.

Using oxalate solution as a precipitation reagent for the synthesis of precursor of transition metal cathodes was studied in 1995 by Prahaharan and co-workers[130]. They used both citrate and oxalate precursors and studied the dependence of the particle size on the annealing temperature.

In 1993 Gao and his group studied about the mechanism of the decomposition of manganese oxalate, which also focused on the annealing process instead of the precursor preparation[131]. Oxalate ions in the solution can play both as the precipitation reagent and the chelating agent. It has also been reported that different types of metal complexes may form under different feed ratio of metal ion and oxalate ion concentration[82]. The formation of metal complexes with oxalate ions as the ligand slows down the precipitation rate and make the nucleation and particle growth process more controllable. According to previous reports, oxalate co-precipitation create precursor particles of narrow size distribution and the particle morphology were successfully adjusted by tuning the solution conditions. Dapeng *et al.* synthesized manganese and lithium-rich cathode materials via oxalate precipitation method[78] using a continuous tank reactor within short residual time. They studied how the pH of the feeding solution influences the composition and morphology of the product and found out that as the pH raised from 1 to 7 the particles transformed from cubical to lamellar shape. Sophie et al. have also synthesized nickel and manganese oxalate powder in continuous flow micro-reactor generated by immiscible organic fluid[132]. They obtained oxalate particles of regular octahedral shape and narrow size distribution from 10 to 12 um. The particle shape and size tunabilities of oxalate co-precipitation makes this synthesis route a better alternative compared to co-precipitation using hydroxide or carbonate as the precipitate agent. However, systematic study about the oxalate precipitation process is still needed to get fundamental knowledge about the equilibrium and kinetic problems in both the single cation precipitation and the mixed cation precipitation. Our goal here is to produce highly performing LNMO by preparing oxalate precursor of the ideal chemical composition. A kinetic study of the precipitation reaction is conducted to get a better understanding of the precipitation process.

2.3. Equilibrium and Kinetic Studies about Co-Precipitation Study

Though being considered as a good tool to synthesize homogeneous phase-pure particles of preferential size and shape, the equilibrium and kinetic studies about the co-precipitation is very rare even for the traditional hydroxide and carbonate co-precipitations. Using TM sulfates and sodium carbonate as precipitating agent and ammonium hydroxide as pH controller and chelating agent, respectively, Gu and his co-workers studied the effect of pH on the physical and electrochemical properties[84]. Among the target pH values of 7.5, 7.8, 8, and 8.3, they found out that pH 8.3, which is also the highest in the series, gave the least Ni and Li site mixing, largest particle size and thus highest tap density, and optimal electrochemical performance. They tried to explain this observation by doing equilibrium calculation and plotted the residual Ni^{2+} and Mn^{2+} concentrations as a function of pH values. Both the TM ion concentrations show a trend to decrease as the pH value increases and they thus claimed that a relationship exists between the residual TM ions and the occupation of Ni^{2+} in the lithium site under different pH values. Such proposal is nearly rude without either theoretical reference or experimental supports. All the physical and chemical factors, such as stoichiometry deviation, crystallinity and phase impurity, are controlled and should be explained by solution chemistry, which needs fundamental knowledge of the reaction mechanism, from both equilibrium and kinetic standpoints. Dapeng and co-workers also studied the carbonate particle growth as a function of reaction time in terms of particle size distribution and chemical composition[85]. They used EDXS to measure the compositions of the particles collected during the co-precipitation. This qualitative analysis showed that the Mn/Ni atomic ratio fluctuated with time early in the process and then became stable after 5 hours. But the stabilized ratio is still noticeably less than the designed ratio and they didn't include the potential effect of this stoichiometry deviation on the electrochemical

properties in their study. In their recent paper about oxalate co-precipitation[78], they showed the reaction pH and ammonia/chelating effects on the precipitate chemical compositions (Mn/Ni ratios), and that the deviation of precipitate composition was caused by solubility differences between nickel oxalate and manganese oxalate. But their study is still based on practical data and a deep understanding of co-precipitation mechanism supported by equilibrium and kinetic data is in great need to better utilize this synthesis route to produce particles of controllable composition and morphology.

3. Materials and Methods

3.1. Preparation of Oxalate Precursor and Cathode Active Material Particles

Laboratory grade $MnSO_4 \cdot H_2O$, $NiSO_4 \cdot 6H_2O$, $Na_2C_2O_4$ (Fisher) were used for the co-precipitation synthesis. Transition metal (TM) sulfate and oxalate reagents were dissolved separately in deionized (DI) water to prepare TM solution and oxalate solution; the TM solution was then poured all at once into the oxalate reagent solution to start the precipitation reaction. The total volumes of the mixed solution were consistently 0.8 L for all sets of synthesis, and the reagent masses were determined by the required solution concentrations and TM feed ratios. Both solutions were preheated to 60 °C prior to mixing and the temperature was maintained during the reaction using a hot plate. The solution was also stirred at 300 rpm with a magnetic stirrer to create a homogeneous mixing condition as the crystallization reaction first initializes and to prevent particles from settling down during the reaction. The particles were collected by vacuum filtering after 30 minutes, and then rinsed with ~2 L DI water before drying in the oven (Carbolite) at 80 °C overnight. The as-above synthesized precursor was well mixed with 5% excess amount of LiOH using a petrol and mortar for 5 minutes. The mixed powder was then fired in the furnace (Carbolite CWF 1300 box furnace) in the air atmosphere at 800°C for 6 hours to obtain $LiMn_{1.5}Ni_{0.5}O_4$. The temperature ramping up speed was set at 1°C / minute, and during the ramping process the temperature was programmed to stay at 200 °C and 350 °C for extra 2 hours, respectively, to allow the structural water loss and oxidation reaction to take place completely.

3.2. Co-precipitation Kinetic Data Collection

Kinetic data was collected using the 1L beakers as the reactor, the same as the normal synthesis route. The solution sample was collected using a 3 mL syringe and the solvent was separated from the solid precipitate using a 33 mm syringe filter of 0.22 um pore size (Fisherbrand). The solvent was further digested using aqua regia and diluted with DI water into a proper concentration for ICP analysis (PerkinElmer Optima 8000). Solution samples were continuously collected along the course of the reaction and the TM concentrations as a function of reaction time plot was obtained. The equilibrium calculations are conducted using OLI^{TM} Studio 9.2.

3.3. Material Characterization and Electrochemical Performance Tests

The chemical compositions of the precursors was measured using ICP analysis after the powders were digested using aqua regia and diluted into proper concentrations. The oxalate precursor and cathode material morphology were characterized with a scanning electron microscope (SEM, FEI Quanta 650). The crystal structure of the material was analyzed by powder X-ray diffraction with a PANalytical X'pert ProMPD using a Cu-Kα radiation source. Thermal gravimetrical analysis (TGA, TA Q50) was also conducted to confirm the amount of the structural water and the weight loss profile of the oxalate precursors. All thermal measurements were performed in air at a heating rate of 10°C min^{-1}. Electrochemical testing was performed using CR2032 coin-type cells. The cathodes were fabricated by blending 80 wt% LiMn$_{1.5}$Ni$_{0.5}$O$_4$, 10 wt% acetylene black as the conductive additive, and 10 wt% polyvinylidene difluoride (PVDF) binder (dissolved in N-methyl-2-pyrrolidone (NMP) as the solvent), and the obtained slurry was pasted onto an aluminum foil current collector with AFA-3 automatic thick film coater and dried at 80 °C overnight, followed by another 3 hour vacuum drying at 80 °C prior to punching into 14

mm electrode disks. Cells were assembled inside an argon-filled glove box with lithium metal as the counter anode. Cel-gard 2325 membrane was used as the separator. The electrolyte was 1.2M LiPF6 dissolved in ethylene carbonate (EC) and ethyl methyl carbonate (EMC) (3:7 vol.%). The cells were tested in the voltage range of 3.6–4.9 V at room temperature in a Maccor battery tester.

4. Results and Discussion

4.1. Manganese Nickel Co-Precipitation Kinetic Study

We use co-precipitation method to synthesize blend transition metal precursor, followed by firing the precursor with lithium salt to obtain the transition metal oxide active materials. The advantage of this two-step synthesis procedure, compared to the traditional solid state reaction method, is that the transition metal ions are supposed to get homogeneously distributed in the precursor particles, eliminating the impurity phase formation and phase segregation resulted from the mass transport limit during the solid state reaction process. One of the most important drawbacks when using the co-precipitation synthesis method, however, is the composition deviation of the precursor, which is further passed into the final active materials. The solubility difference between different transition metal precipitates is the main cause of stoichiometry deviation of the solid product compared to the feed ratio of the solution, which is often made the same as the designed ratio. Oxalate is used as the precipitation reagent in our synthesis. In the manganese nickel blend oxalate co-precipitation system, due to the higher solubility of $MnC_2O_4.2H_2O$ than $NiC_2O_4.2H_2O$, the oxalate precipitate is predicted to be Ni rich. The lower the feed concentration is, the higher fraction of feed TM ions will reside in solution when getting close to the equilibrium. Therefore the stoichiometry deviation of precipitates is expected to be more exaggerated in low concentration regime, under which condition the particle morphology control is feasible to achieve. Figure 1 shows the curve of calculated Mn/Ni ratios in the precipitates at equilibrium as a function of feed concentrations. The values of the shown points are also listed in Table A 1. The Mn/Ni ratio drops sharply away from the feed ratio 3:1 as the feed concentration decreases below 50mM. The ratio is 1.7 as the concentration decreases to 10mM, which indicates nearly 50% deviation from the feed ratio. However, as our reaction

duration time is controlled consistently at 30 minutes, which may not be enough for the reaction to reach equilibrium, the kinetic factor is expected to also play an important role in determining the TM ratio in the precipitate. From the thermodynamic aspect, manganese oxalate precipitation reaction has lower energy barrier, thus manganese oxalate crystalizes and precipitates faster than nickel oxalate especially in the beginning period. The curve of measured Mn/Ni ratios of collected powders as a function of feed concentrations is also shown in Figure 2. All the precursors were collected after 30 minute duration time. Compared to the values from equilibrium calculation, the measured ratios are relatively higher especially in low concentration regime. This implies that the kinetic influence resulted from the faster manganese oxalate precipitation rate compensates for the composition deviation under equilibrium condition if short reaction time is applied. As the concentration increases, the difference between the measured values and the calculate values become less as the system requires less time to reach equilibrium.
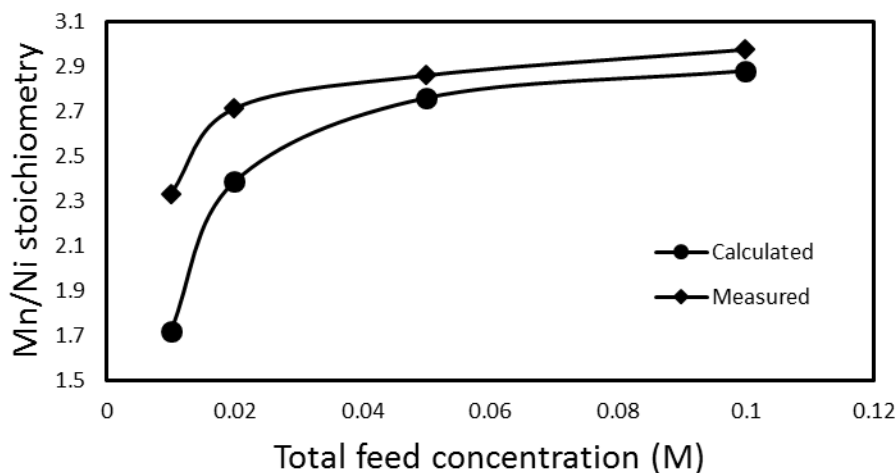

Figure 2. The calculated and measured Mn/Ni stoichiometries in the precipitate as a function of total feed concentration. The feed ratios of Mn/Ni are 3/1.

We then carefully study the solution chemistry of the 20mM batch, aiming to get the stoichiometrically correct precipitate by tuning the feed TM ratio. Figure 3 a) and b) show the kinetic curves of pure Mn oxalate and Ni oxalate precipitation, respectively. It can be seen that Mn ion concentration drops faster than Ni ion, while at the end of the reaction period the concentration of residual Ni ion is more close to zero. Quantitatively, Mn ion concentration stabilizes at around 0.0045 mol/L after 25 minutes, which corresponds to 77% conversion rate. In comparison, Ni ion concentration keeps dropping even after 60 minutes, with the residual concentration to be 0.00265 mol/L after 67 minutes (point not shown in the curve), which corresponds to 87% conversion rate. It is also worth mentioning that after 30 minutes for the pure Ni oxalate precipitation, the ion concentration is about 0.0079 mol/L which gives only 60% conversion rate. Therefore by looking at the kinetic plots of the pure TM oxalate precipitations, the precipitate from the blend precipitation should be Mn rich if collected after 30 minutes, and it should be Ni rich if collected after 60 minutes, based on the reaction conversion rates of the two TMs. In the Mn/Ni 3/1blend system, however, similar kinetic curves of the two TM precipitations are observed, indicating that both the precipitation rates and reaction extents of the two TM ions resemble each other (Figure 3 plot c)). This implies the interaction of the two TM precipitations in the co-precipitation process. In Figure 3 d) the reaction extent in the form of precipitation percentage versus reaction time plot shows clearly that both Mn oxalate and Ni oxalate precipitations reach plateaus nearly simultaneously after around 20 minutes, unlike in the pure Ni oxalate where the ion concentration keeps dropping down gradually till the reaction ends. 87% of manganese ion and 92% of nickel ion participate in the reaction and enter into the precipitate in the blend reaction after 30 minutes, compared to the precipitation rates of 77% and 60% in their pure oxalate precipitation reactions, respectively. The co-precipitation interaction

causes the precipitated fractions for both the two ions to increase and the kinetic and equilibria differences between the two precipitation reactions to decrease significantly. The co-precipitation reaction turns out to be more complete and also contains less composition deviation compared to the simple mix condition where only reaction kinetic and equilibria factors are considered. Our speculation is that 1) the first crystallized Mn oxalate particles could provide seeds to facilitate Ni oxalate precipitation and 2) the more stable Ni oxalate structure gives a preferred backbone to facilitate Mn oxalate precipitation.
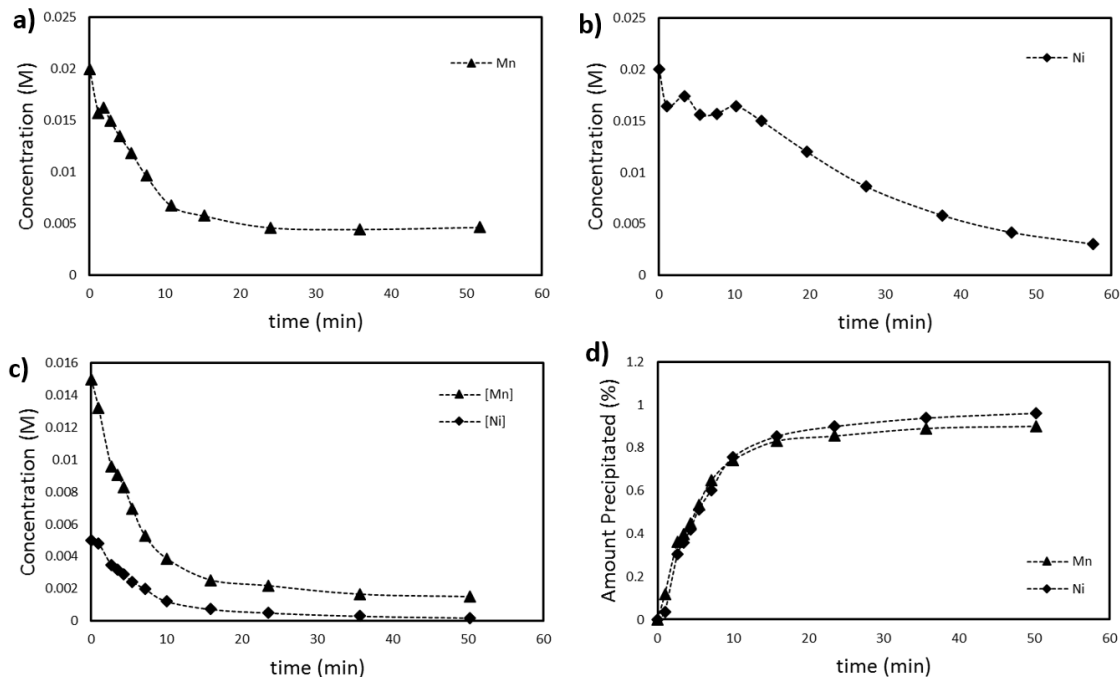
Figure 3. Kinetic curves of a) pure manganese oxalate precipitation, b) pure nickel oxalate precipitation, and c) Mn/Ni 3/1 co-precipitation. The concentrations of TM and oxalate solutions are all 20mM. Percentage of precipitated TM ions as a function of reaction are shown in d) to easier compare the reaction extents of manganese and nickel ions with different feed concentrations in the co-precipitation reaction shown in plot c).

The first speculation is supported by our seeding experiment, where we added 10 atm % of manganese oxalate seeds into the nickel oxalate precipitation batch as the TM solution and the oxalate solution were mixed together. The kinetic curves of the seeding batch, of the pure nickel control batch, and of the Mn/Ni 3/1 batch are shown in Figure 4. The total TM feed concentrations are 20mM in all these three batches. It can be seen from plot a) that adding manganese seeds facilitates the precipitating of nickel oxalate, with the nickel ion concentration dropping down faster than in the control batch. From plot b) we can see that the precipitation rate of nickel oxalate in the seeding batch is still slower than in the Mn/Ni 3/1 batch. We attribute the difference to the higher quantity of the manganese oxalate seeds in the blend system, specifically, the more available surface area of the seeds as the nucleation and crystallization first occurs.
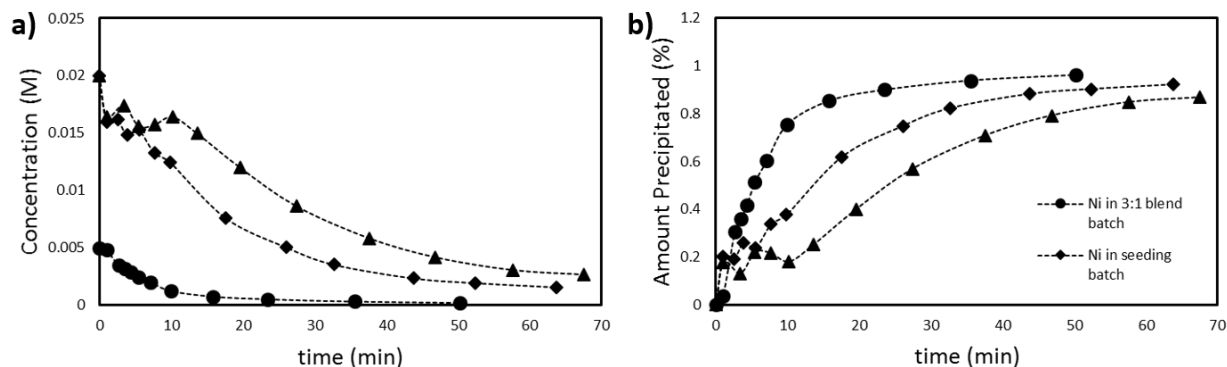

Figure 4 a) The kinetic curves of Ni ions in Mn/Ni 3/1 blend batch, pure Ni precipitation batch, and Ni precipitation batch with MnC2O4.2H2O seeds; and b) the reaction extents in the form of precipitation percentage for the corresponding three batches.

The SEM image of the manganese seeds is shown in Figure A 2 a). The particles are found to be aggregates of primary particles, with the average size of around 20um and much reduced surface/volume or surface/mass ratio, thus may render the exposed surface area less compared to the newly crystallized particles. Quantitative comparison in the surface areas of the seeds

23

between these two batches may be conductible using BET tests but is not done at the current stage. The second speculation that nickel provides a stable backbone for manganese oxalate precipitation can be partially supported by the X-Ray diffraction patterns of the pure and blend TM oxalate powders, shown in Figure 5. The X-Ray pattern of the blend TM oxalate particle is iso-structural to the pattern of nickel oxalate powder, even though all the peaks are less sharp and intense. The peaks of the blend powder also show left shifting compared to the peaks of pure nickel oxalate powder, which indicates the expansion of lattice due to the larger size manganese ions intercalating into the structure.
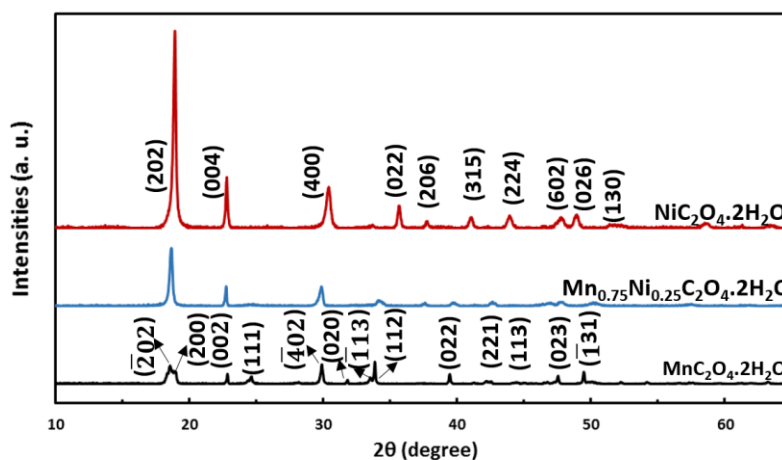
Figure 5. XRD patterns of manganese oxalate, nickel oxalate, and 3:1 manganese nickel blend oxalate powders. The patterns are Miller indexed with orthorhombic and monoclinic symmetries for nickel oxalate powder and manganese oxalate powder, respectively.

TGA analyses are also conducted on these three samples and the results are shown in Figure 6. The weight drop before 200 °C due to the structural water lost, are all around 20 % for the three samples, which implies that the oxalates all contains 2 structural waters in the formula, expressed as $MnC_2O_4.2H_2O$, $NiC_2O_4.2H_2O$, and $Mn_{0.75}Ni_{0.25}C_2O_4.2H_2O$, respectively. For $MnC_2O_4.2H_2O$ there are two weight loss peaks at 272 °C and 441 °C, with weight loss percentages of 54.72 %

and 55.98 %, respectively. These numbers, compared with the theoretical values being 51.4 % (MnO_2), 55.9 % (Mn_2O_3), 57.38 % (Mn_3O_4), and 60.35 % (MnO), indicate that the manganese oxalate dihydrate was oxidized into a mixture of MnO_2 and Mn_2O_3 after the first peak before 300 °C and then the residual Mn^{4+} ions are reduced into Mn^{3+} status after the 441 °C peak, accompanied by oxygen loss. Nickel oxalate dihydrate lost around 59 % of weight after the 316 °C peak, which corresponds to the oxidation into NiO (theoretical value being 59.13 %). The temperature of structural water loss is higher for $NiC_2O_4.2H_2O$ than for $MnC_2O_4.2H_2O$, which is another proof that the crystal structure of $NiC_2O_4.2H_2O$ is more stable than $MnC_2O_4.2H_2O$, thus is preferred in the blend system. From the TGA curve of $Mn_{0.75}Ni_{0.25}C_2O_4.2H_2O$ shown in plot Figure 6 c), we see that the structure water loss temperature is between those of the two pure transition metal oxalate dihydrates while closer to that of $NiC_2O_4.2H_2O$. This also points to the direction that the blend oxalate is isotropical to $NiC_2O_4.2H_2O$, which is more structural stable.
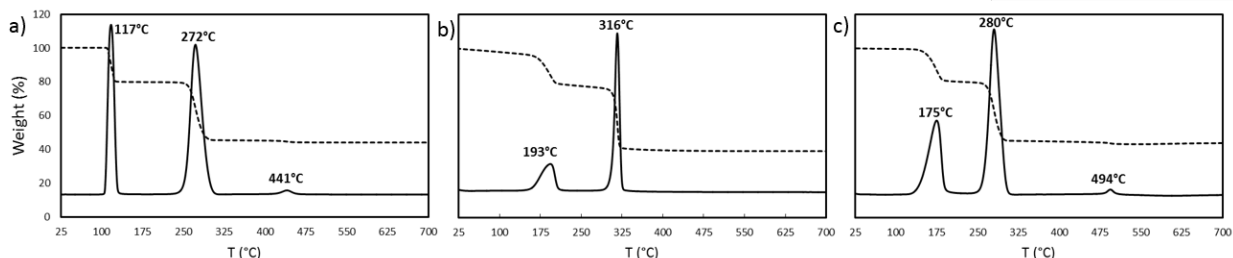

Figure 6 TGA analysis of a) MnC2O4.2H2O, b) NiC2O4.2H2O, and c) Mn0.75Ni0.25C2O4.2H2O.

Due to the interplay of equilibrium and kinetic factors in the system, the qualitative explanation of the interaction between different TM precipitations, and also the limited accuracy of the current data, it is difficult to raise a module to predict the stoichiometry of a collected powder under a certain condition. Table 1 lists the calculated and measured TM ratios of the precipitate

from different feed ratios with 20mM as the total TM feed concentration. The deviation percentages of the measured values from the calculated values are consistent, given the fact that nucleation process is also influenced by many trivial factors including the surface smoothness of the reactor and the impurity amount of the solvent, which are hard to control. We see from the table that the 3.5 feed ratio gives the correct Mn/Ni in the precipitate. Either higher or lower feed ratio render the precipitate non-stoichiometric, giving Mn rich or Ni rich precursor and LNMO. The chemical formulas of the corresponding LNMO samples are also shown in the table, assuming that the lithium amount is one half of the TM amount in moles. $LiMn_{1.47}Ni_{0.53}O_4$, $LiMn_{1.50}Ni_{0.50}O_4$, and $LiMn_{1.54}Ni_{0.46}O_4$ are further studied, representing nickel rich, stoichiometric, and manganese rich LNMO, respectively.

Table 1. The feed ratios of precipitation solutions and the resulted Mn/Ni stoichiometry in the precipitate from equilibrium calculation and ICP measurement

Feed ratio	Equilibrium Calculation	Measured using ICP	Deviation (%)	Chemical Formula of LNMO
3.00	2.38	2.60	8.87	$LiMn_{1.47}Ni_{0.53}O_4$
3.52	2.85	3.02	5.85	$LiMn_{1.50}Ni_{0.50}O_4$
3.65	2.97	3.28	10.8	$LiMn_{1.53}Ni_{0.47}O_4$
3.82	3.11	3.33	7.18	$LiMn_{1.54}Ni_{0.46}O_4$

4.2. Characterization of the Stoichiometric and Non-stoichiometric High Voltage Spinel

Figure A 3 show the SEM images of the three precursors and their corresponding LNMO samples. It can be seen that all the precursors exhibit octahedral shape and similar particle size of about 20 μm. The octahedral shape of the precursor are retained for LNMOs. The LNMO sample images are further zoomed in to show detailed morphologies in Figure A 3 g-i). From these high-resolution SEM images of LNMO, we can see the octahedral secondary particles are comprised of nanometer-sized multi-faceted primary particles. The pores are generated by the release of structural water and carbon dioxide produced during oxalate decomposition in the calcination process. The nanometer-sized primary particles expose more surface area for the cathode-electrolyte electron exchange and surface reaction. The pores between the primary particles connect to form internal channels in which electrolyte is able to diffuse in and contact with the electrode. This channel structure also leads to high loading in electrode processing and is able to better accommodate the volume change and to reduce the electrode tension upon cycling. Therefore, the overall morphology of our synthesized particles is found to be beneficial for fast Li ion and electron transport during charge and discharge.
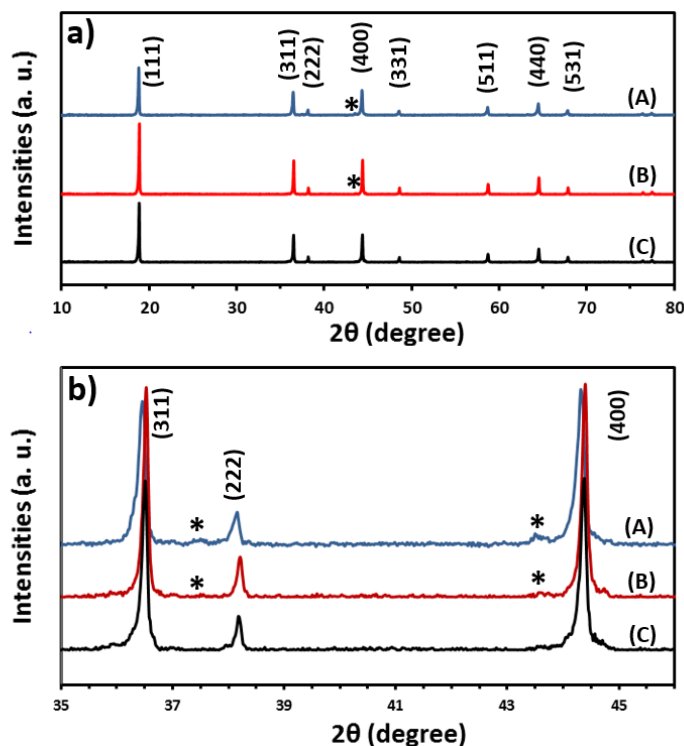
Figure 7. The XRD patterns of (A) manganese rich, (B) stoichiometric, and (C) nickel rich LNMOs. The patterns are zoomed in to better show the rock-salt impurity phase (marked with *) in plot b).

X-Ray Diffraction was conducted on the nickel rich, stoichiometric, and manganese rich LNMO powders and the patterns are shown in Figure 7. The peaks all fit well with the spinel cubic structures. In the patterns of the nickel rich and stoichiometric samples, peaks from the impurity nickel rich phase (reported to be $LiNiO_2$ with layered structure) are present, but not in the manganese rich LNMO pattern. The impurity peaks are also more intense in the nickel rich sample than in the stoichiometric sample, which is detrimental to the cycling performance of the cell due to its poor ionic and electronic conductivity. This implies that higher nickel fraction in the LNMO structure facilitates the formation of the rock-salt impurity phase, even though the impurity phase could also exist in the stoichiometric LNMO. The manganese rich LNMO sample

is found to be free of the impurity phase; however, it may render the whole structure less stable with extensive amount of Mn^{3+} existent in the structure.
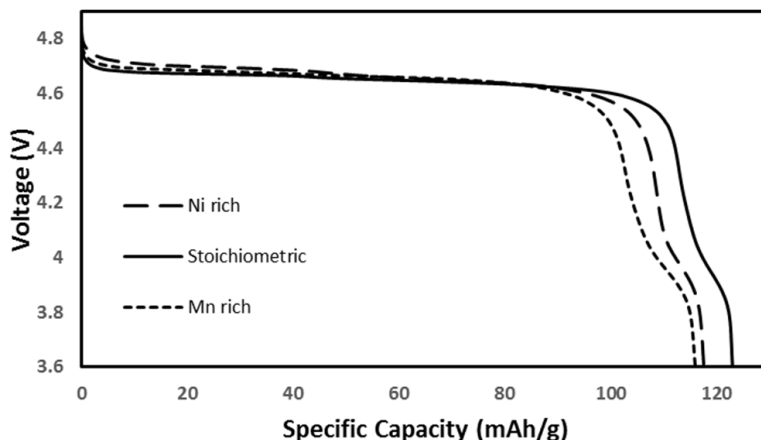

Figure 8. Discharge profiles of manganese rich, stoichiometric, and nickel rich LNMOs. Cells are discharged at C/10 rate.

The discharge curves of the cells composed of the three samples, discharged all at C/10, are shown in Figure 8. The stoichiometric LNMO shows the highest total capacity of 123 mAh/g, while the manganese or nickel rich LNMO show similar capacities of around 115 mAh/g. Dividing the voltage into high and low voltage range and corresponding each range to Ni^{2+}/Ni^{4+} and Mn^{3+}/Mn^{4+} redox couples, Table 2 lists the capacities of the three samples in the high voltage and low voltage range, and also their percentages among the total capacities and the calculated Mn^{3+} amounts based on the capacities in the low voltage range. It is seen that the low voltage capacities of the Ni rich LNMO and stoichiometric LNMO are close, with their percentages among the total capacities and the calculated Mn^{3+} amounts identical. This is attributed to the Mn^{3+} formation during our high temperature calcination procedure, regardless of the composition of the samples. The TGA test also shows that Mn ions tend to be reduced to

Mn^{3+} as the temperature rises up beyond 300°C. The capacity reduction of the nickel rich LNMO, compared with the stoichiometric LNMO, is thus resulted from the high voltage capacity decrease, which can be explained by the rock-salt phase formation. The manganese rich LNMO contains higher percentage of low voltage capacity, due to the higher amount of Mn^{3+} in the structure. Expressing the Mn rich structure as $LiNi_x^{2+}Mn_{1-2x}^{3+}Mn_{1+x}^{4+}O_4$, we know x equals 0.46, and the composition is thus expected to be $LiNi_{0.46}^{2+}Mn_{0.08}^{3+}Mn_{1.46}^{4+}O_4$ with 5.19% Mn at +3 status among the structure. By comparison, the Mn^{3+} percentage calculated based on the low voltage range capacity is 5.27%, which is close to the theoretical prediction. Then we compare the high voltage range capacities of the Mn rich LNMO and stoichiometric LNMO. Assuming that all the high voltage capacities come from the Ni^{2+}/Ni^{4+} redox couple, Ni^{2+} amounts are calculated and listed also in the table. Even in the stoichiometric sample, the Ni^{2+}/Ni^{4+} redox couple cannot be fully exploited during charge or discharge, due to the nickel-rich impurity phase formation and the intrinsic structure intercalation limit. However, if we compare the calculated Ni^{2+} amount of the manganese rich sample and that of the stoichiometric sample, the ratio is 0.91, which is very close to the theoretical Ni^{2+} ratio of 0.92 obtained by comparing $LiNi_{0.46}^{2+}Mn_{0.08}^{3+}Mn_{1.46}^{4+}O_4$ to $LiNi_{0.5}Mn_{1.5}O_4$. This implies that the capacity loses caused by impurity phase formation and structural intercalation limit occupies a certain fraction of the total theoretical capacities. The chemical composition of LNMO sample may be successfully used to predict the high voltage and low voltage range capacity, knowing the stoichiometric discharge data as the benchmark.

Table 2. Summaries of the nickel rich, stoichiometric, and manganese rich LNMO discharge profiles

Sample	Formula	Specific Capacity/ mAh/g			Mn/mol	Ni/mol	Capacity Percentage/%	
		Total	Low Voltage	High Voltage			Low Voltage	High Voltage
Nickel Rich	$LiMn_{1.47}Ni_{0.53}O_4$	117.56	8.67	108.89	0.0591	0.371	7.38	92.62
Stoichiometric	$LiMn_{1.50}Ni_{0.50}O_4$	123.05	9.04	114.01	0.0616	0.389	7.35	90.96
Manganese Rich	$LiMn_{1.54}Ni_{0.46}O_4$	115.99	11.91	104.08	0.0812	0.355	10.27	88.09

Cycling performance tests were also conducted on the three cells and the plots are shown in Figure A 4. None of the three cells show significant capacity fade after charging and discharging at C/10 for 50 cycles. This could be attributed to the nano-sized active particles and the pore-channel morphology of the primary particles, which facilitate fast charge and ion transfer and stabilize the particle structure, and slows down the fading rate caused by phase impurity and structure distortion. The comparison in cycle life and capacity retention among the stoichiometric and non-stoichiometric LNMOs should be conducted after more charge-discharge cycles.

5. Conclusions

Kinetic study was successfully conducted for the manganese nickel oxalate co-precipitation reactions. Compared to the pure TM oxalate precipitations, the precipitations proceed more complete for both of the two TM ions in the blend system. The interaction between the two TM ion precipitation processes also tend to eliminate the difference between the two TM precipitation reactions from both thermodynamic and equilibrium aspects. The two TM ions tend to precipitate at similar speeds and the precipitated percentages among the total feed after a certain duration time are getting much closer compared to the pure precipitation reactions. This interaction being considered, we successfully synthesized the stoichiometrically correct precursor and the final LNMO, by tuning the feed ratio of the co-precipitation reaction. The discharge capacity of the stoichiometric LNMO is shown to be higher than both the manganese and nickel rich LNMOs, which corresponds well with the theoretical analysis and again emphasizes the importance of correct stoichiometry of the TM oxide active materials in Li-ion battery cathode material application. Our study uses oxalate co-precipitation and the high voltage spinel specifically as a representative of the idea. Similar study can also be done to co-precipitation systems using other precipitation reagents, and be used to adjust the stoichiometry of other type of TM oxide cathode materials.

References

1. Lee, E., Nam, K.-W., Hu, E. & Manthiram, A. Influence of Cation Ordering and Lattice Distortion on the Charge-Discharge Behavior of LiMn1.5Ni0.5O4 Spinel between 5.0 and 2.0V. *Chem. Mater.* **24,** 3610–3620 (2012).

2. Casas-Cabanas, M., Kim, C., Rodriguez-Carvajal, J. & Cabana, J. Atomic scale drivers of ordering transitions in LiNi0.5Mn1.5O4 and relationship with electrochemical properties. *J. Mater. Chem. A* 8255–8262 (2016). doi:10.1039/C6TA00424E

3. Kozawa, T., Murakami, T. & Naito, M. Insertion of lattice strains into ordered LiNi0.5Mn1.5O4 spinel by mechanical stress: A comparison of perfect versus imperfect structures as a cathode for Li-ion batteries. *J. Power Sources* **320,** 120–126 (2016).

4. Saravanan, K., Jarry, A., Kostecki, R. & Chen, G. A study of room-temperature LixMn1.5Ni0.5O4 solid solutions. *Sci. Rep.* **5,** 8027 (2015).

5. Duncan, H., Hai, B., Leskes, M., Grey, C. P. & Chen, G. Relationships between Mn 3+ Content, Structural Ordering, Phase Transformation, and Kinetic Properties in LiNi x Mn 2– x O 4 Cathode Materials. *Chem. Mater.* **26,** 5374–5382 (2014).

6. High voltage spinel oxides for Li ion batteries From the material research to the application.

7. Thackeray, M. M., Johnson, C. S., Vaughey, J. T., Li, N. & Hackney, S. A. Advances in manganese-oxide 'composite' electrodes for lithium-ion batteries. *J. Mater. Chem.* **15,** 2257–2267 (2005).

8. Kang, S.-H. *et al.* Interpreting the structural and electrochemical complexity of 0.5Li2MnO3[middle dot]0.5LiMO2 electrodes for lithium batteries (M = Mn0.5-Ni0.5-

Co2, 0 [less-than-or-equal] x [less-than-or-equal] 0.5). *J. Mater. Chem.* **17,** 2069–2077 (2007).

9.   Kang, S.-H., Johnson, C. S., Vaughey, J. T., Amine, K. & Thackeray, M. M. The Effects of Acid Treatment on the Electrochemical Properties of 0.5 Li2MnO3 · 0.5 LiNi0.44Co0.25Mn0.31O2 Electrodes in Lithium Cells. *J. Electrochem. Soc.* **153,** A1186–A1192 (2006).

10.   Kim, J.-S., Johnson, C. . & Thackeray, M. . *Layered xLiMO2·(1−x)Li2M'O3 electrodes for lithium batteries: a study of 0.95LiMn0.5Ni0.5O2·0.05Li2TiO3*. *Electrochemistry Communications* **4,** (2002).

11.   Kim, D., Kang, S.-H., Balasubramanian, M. & Johnson, C. S. *High-energy and high-power Li-rich nickel manganese oxide electrode materials*. *Electrochemistry Communications* **12,** (2010).

12.   Zheng, J. *et al.* Functioning Mechanism of AlF3 Coating on the Li- and Mn-Rich Cathode Materials. *Chem. Mater.* **26,** 6320–6327 (2014).

13.   Hwang, S. *et al.* Using Real-Time Electron Microscopy To Explore the Effects of Transition-Metal Composition on the Local Thermal Stability in Charged LixNiyMnzCo1−y–zO2 Cathode Materials. *Chem. Mater.* **27,** 3927–3935 (2015).

14.   Yang, F. *et al.* Nanoscale Morphological and Chemical Changes of High Voltage Lithium–Manganese Rich NMC Composite Cathodes with Cycling. *Nano Lett.* **14,** 4334–4341 (2014).

15.   Li, J. *et al. Synthesis and electrochemical performance of the high voltage cathode*

material Li[Li0.2Mn0.56Ni0.16Co0.08]O2 with improved rate capability. *Journal of Power Sources* **196,** (2011).

16. Mohanty, D. *et al.* Structural transformation of a lithium-rich Li1.2Co0.1Mn0.55Ni0.15O2 cathode during high voltage cycling resolved by in situ X-ray diffraction. *J. Power Sources* **229,** 239–248 (2013).

17. Lee, I. *et al.* Communication—Preparation of Highly Monodisperse Ni-Rich Cathode Material for Lithium Ion Batteries. *J. Electrochem. Soc.* **163,** A1336–A1339 (2016).

18. Robert, R., Bünzli, C., Berg, E. J. & Novák, P. Activation Mechanism of LiNi0.80Co0.15Al0.05O2: Surface and Bulk Operando Electrochemical, Differential Electrochemical Mass Spectrometry, and X-ray Diffraction Analyses. *Chem. Mater.* **27,** 526–536 (2015).

19. Wu, N., Wu, H., Liu, H. & Zhang, Y. Solvothermal coating LiNi0.8Co0.15Al0.05O2 microspheres with nanoscale Li2TiO3 shell for long lifespan Li-ion battery cathode materials. *J. Alloys Compd.* **665,** 48–56 (2016).

20. Hwang, S. *et al.* Investigation of Changes in the Surface Structure of LixNi0.8Co0.15Al0.05O2 Cathode Materials Induced by the Initial Charge. *Chem. Mater.* **26,** 1084–1092 (2014).

21. Dogan, F., Vaughey, J. T., Iddir, H. & Key, B. Direct Observation of Lattice Aluminum Environments in Li Ion Cathodes LiNi1−y−zCoyAlzO2 and Al-Doped LiNixMnyCozO2 via 27Al MAS NMR Spectroscopy. *ACS Appl. Mater. Interfaces* **8,** 16708–16717 (2016).

22. Liu, G., Park, K.-S., Song, J. & Goodenough, J. B. Influence of thermal history on the

electrochemical properties of Li[Ni0.5Mn1.5]O4. *J. Power Sources* **243,** 260–266 (2013).

23. Hu, M., Pang, X. & Zhou, Z. Recent progress in high-voltage lithium ion batteries. *J. Power Sources* **237,** 229–242 (2013).

24. Kunduraci, M. & Amatucci, G. G. The effect of particle size and morphology on the rate capability of 4.7 V LiMn1.5+??Ni0.5-??O4 spinel lithium-ion battery cathodes. *Electrochim. Acta* **53,** 4193–4199 (2008).

25. Goodenough, J. B. & Park, K. S. The Li-ion rechargeable battery: A perspective. *J. Am. Chem. Soc.* **135,** 1167–1176 (2013).

26. Goodenough, J. B. & Kim, Y. Challenges for rechargeable Li batteries. *Chem. Mater.* **22,** 587–603 (2010).

27. Yi, T. F., Mei, J. & Zhu, Y. R. Key strategies for enhancing the cycling stability and rate capacity of LiNi0.5Mn1.5O4 as high-voltage cathode materials for high power lithium-ion batteries. *J. Power Sources* **316,** 85–105 (2016).

28. Noorden, R. Van. The rechargeable revolution: A better battery. *Nature* **507,** 26–28 (2014).

29. Julien, C. M. & Mauger, A. *Review of 5-V electrodes for Li-ion batteries: Status and trends. Ionics* **19,** (2013).

30. Liu, D., Han, J. & Goodenough, J. B. Structure, morphology, and cathode performance of Li1-x[Ni0.5Mn1.5]O4 prepared by coprecipitation with oxalic acid. *J. Power Sources* **195,** 2918–2923 (2010).

31. Belak, A. A. Understanding Li Diffusion in Li-Intercalation.pdf. **XXX,** (2011).

32.   Liu, D. *et al.* Spinel materials for high-voltage cathodes in Li-ion batteries. *Rsc Adv.* **4,** 154–167 (2014).

33.   Wang, L., Li, H., Huang, X. & Baudrin, E. A comparative study of Fd-3m and P4332 'LiNi0.5Mn1.5O4'. *Solid State Ionics* **193,** 32–38 (2011).

34.   Chemelewski, K. R., Lee, E. S., Li, W. & Manthiram, A. Factors influencing the electrochemical properties of high-voltage spinel cathodes: Relative impact of morphology and cation ordering. *Chem. Mater.* **25,** 2890–2897 (2013).

35.   Patoux, S. *et al.* High voltage spinel oxides for Li-ion batteries: From the material research to the application. *J. Power Sources* **189,** 344–352 (2009).

36.   Deng, Y.-F., Zhao, S.-X., Xu, Y.-H., Gao, K. & Nan, C.-W. Impact of P-Doped in Spinel LiNi0.5Mn1.5O4 on Degree of Disorder, Grain Morphology, and Electrochemical Performance. *Chem. Mater.* **27,** 7734–7742 (2015).

37.   Fey, G. T.-K., Lu, C.-Z. & Kumar, T. P. Preparation and electrochemical properties of high-voltage cathode materials, LiMyNi0.5−yMn1.5O4 (M=Fe, Cu, Al, Mg; y=0.0–0.4). *J. Power Sources* **115,** 332–345 (2003).

38.   Shen, L., Li, H., Uchaker, E., Zhang, X. & Cao, G. General Strategy for Designing Core–Shell Nanostructured Materials for High-Power Lithium Ion Batteries. *Nano Lett.* **12,** 5673–5678 (2012).

39.   Wang, L., Maxisch, T. & Ceder, G. A First-Principles Approach to Studying the Thermal Stability of Oxide Cathode Materials. *Chem. Mater.* **19,** 543–552 (2007).

40.   Yabuuchi, N., Makimura, Y. & Ohzuku, T. Solid-State Chemistry and Electrochemistry of

LiCo1∕3Ni1∕3Mn1∕3O2 for Advanced Lithium-Ion Batteries: III. Rechargeable Capacity and Cycleability . *J. Electrochem. Soc.* **154,** A314–A321 (2007).

41.   Yabuuchi, N., Yoshii, K., Myung, S.-T., Nakai, I. & Komaba, S. Detailed Studies of a High-Capacity Electrode Material for Rechargeable Batteries, Li2MnO3−LiCo1/3Ni1/3Mn1/3O2. *J. Am. Chem. Soc.* **133,** 4404–4419 (2011).

42.   Belharouak, I., Koenig, G. M. & Amine, K. Electrochemistry and safety of Li4Ti5O12 and graphite anodes paired with LiMn2O4 for hybrid electric vehicle Li-ion battery applications. *J. Power Sources* **196,** 10344–10350 (2011).

43.   Brochu, F. *et al.* Structure and electrochemistry of scaling nano C–LiFePO4 synthesized by hydrothermal route: Complexing agent effect. *J. Power Sources* **214,** 1–6 (2012).

44.   Wu, F., Wang, M., Su, Y., Bao, L. & Chen, S. *A novel method for synthesis of layered LiNi1/3Mn1/3Co1/3O2 as cathode material for lithium-ion battery*. *Journal of Power Sources* **195,** (2010).

45.   Liu, J., Jiang, R., Wang, X., Huang, T. & Yu, A. *The defect chemistry of LiFePO4 prepared by hydrothermal method at different pH values*. *Journal of Power Sources* **194,** (2009).

46.   Wu, F. *et al.* Synthesis and characterization of hollow spherical cathode Li1.2Mn0.54Ni0.13Co0.13O2 assembled with nanostructured particles via homogeneous precipitation-hydrothermal synthesis. *J. Power Sources* **267,** 337–346 (2014).

47.   Deng, S. *et al.* Preparation and electrochemical properties of double-shell LiNi0.5Mn1.5O4 hollow microspheres as cathode materials for Li-ion batteries. *RSC Adv.*

6, 45369–45375 (2016).

48. Doi, T., Iriyama, Y., Abe, T. & Ogumi, Z. Electrochemical Insertion and Extraction of Lithium Ion at Uniform Nanosized Li4/3Ti5/3O4 Particles Prepared by a Spray Pyrolysis Method. *Chem. Mater.* **17,** 1580–1582 (2005).

49. Huang, X. *et al.* Spray drying-assisted synthesis of hollow spherical Li2FeSiO4/C particles with high performance for Li-ion batteries. *Solid State Ionics* **278,** 203–208 (2015).

50. Li, T. *et al. Electrochemical properties of LiNi0.6Co0.2Mn0.2O2 as cathode material for Li-ion batteries prepared by ultrasonic spray pyrolysis*. *Materials Letters* **159,** (2015).

51. Pişkin, B. & Aydinol, M. K. Development and characterization of layered Li(NixMnyCo1−x−y)O2 cathode materials for lithium ion batteries. *Int. J. Hydrogen Energy* **41,** 9852–9859 (2016).

52. Boyle, T. J. *et al.* A Novel Family of Structurally Characterized Lithium Cobalt Double Aryloxides and the Nanoparticles and Thin Films Generated Therefrom. *Chem. Mater.* **15,** 3903–3912 (2003).

53. Park, J. S., Mane, A. U., Elam, J. W. & Croy, J. R. Amorphous Metal Fluoride Passivation Coatings Prepared by Atomic Layer Deposition on LiCoO2 for Li-Ion Batteries. *Chem. Mater.* **27,** 1917–1920 (2015).

54. Park, J. S. *et al.* Ultrathin Lithium-Ion Conducting Coatings for Increased Interfacial Stability in High Voltage Lithium-Ion Batteries. *Chem. Mater.* **26,** 3128–3134 (2014).

55. Sugiawati, V. A., Vacandio, F., Eyraud, M., Knauth, P. & Djenizian, T. Porous

NASICON-Type Li3Fe2(PO4)3 Thin Film Deposited by RF Sputtering as Cathode Material for Li-Ion Microbatteries. *Nanoscale Res. Lett.* **11,** 365 (2016).

56. Qi, Z. & Koenig, G. M. High-Performance LiCoO2 Sub-Micrometer Materials from Scalable Microparticle Template Processing. *ChemistrySelect* **1,** 3992–3999 (2016).

57. Ma, G. *et al.* A General and Mild Approach to Controllable Preparation of Manganese-Based Micro- and Nanostructured Bars for High Performance Lithium-Ion Batteries. *Angew. Chemie - Int. Ed.* 3667–3671 (2016). doi:10.1002/anie.201511196

58. JeanDubernat & HenriPezerat. Fautes d'Empilement dans les Oxalates Dihydrat6s des M6taux Divalents de la S6rie Magn6sienne (Mg,Fe,Co,Ni,Zn,Mn). *J. Appl. Cryst.* **7,** 387–393 (1974).

59. Amine, K., Tukamoto, H., Yasuda, H. & Fujita, Y. Preparation and electrochemical investigation of LiMn2 − xMexO4 (Me: Ni, Fe, and x = 0.5, 1) cathode materials for secondary lithium batteries. *J. Power Sources* **68,** 604–608 (1997).

60. Lethbridge, Z. A. D., Congreve, A. F., Esslemont, E., Slawin, A. M. Z. & Lightfoot, P. Synthesis and structure of three manganese oxalates: MnC2O4??2H2O, [C4H8(NH2)2][Mn2(C 2O4)3] and Mn2(C2O4)(OH)2. *J. Solid State Chem.* **172,** 212–218 (2003).

61. Sledzinska, I., Murasik, A. & Fischer, P. Magnetic ordering of the linear chain system manganese oxalate dihydrate investigated by means of neutron diffraction and bulk magnetic measurements. *J. Phys. C Solid State Phys.* **20,** 2247–2259 (1987).

62. Ma, C. *et al.* Preparation and characterization of Ni0.6Mn2.4O4 NTC ceramics by solid-

state coordination reaction. *J. Mater. Sci. Mater. Electron.* **24,** 5183–5188 (2013).

63.   Ahmad, T., Ganguly, A., Ahmed, J., Ganguli, A. K. & Alhartomy, O. A. A. Nanorods of transition metal oxalates: A versatile route to the oxide nanoparticles. *Arab. J. Chem.* **4,** 125–134 (2011).

64.   Mukherjee, A. K. Human Kidney Stone Analysis using X-ray Powder Diffraction. **94,** (2014).

65.   Donkova, B. & Mehandjiev, D. Mechanism of decomposition of manganese(II) oxalate dihydrate and manganese(II) oxalate trihydrate. *Thermochim. Acta* **421,** 141–149 (2004).

66.   Drouet, C., Alphonse, P. & Rousset, A. Synthesis and characterization of non-stoichiometric nickel-copper manganites. *Solid State Ionics* **123,** 25–37 (1999).

67.   April, R., Jonker, C. G. H. & Huizing, A. Pergamon Press , Inc . P r i n ~ d i n t h e. **12,** 605–611 (1977).

68.   Wang, D., Belharouak, I., Zhou, G. & Amine, K. Synthesis of Lithium and Manganese-Rich Cathode Materials via an Oxalate Co-Precipitation Method. *J. Electrochem. Soc.* **160,** A3108–A3112 (2013).

69.   Liu, H. *et al.* Controllable synthesis of spinel lithium nickel manganese oxide cathode material with enhanced electrochemical performances through a modified oxalate co-precipitation method. *J. Power Sources* **274,** 1180–1187 (2015).

70.   Zhang, L., Borong, W., Ning, L. & Feng, W. Hierarchically porous micro-rod lithium-rich cathode material Li1.2Ni0.13Mn0.54Co0.13O2 for high performance lithium-ion batteries. *Electrochim. Acta* **118,** 67–74 (2014).

71.   Shi-xuan, L. Micro / Nanostructure and High Rate Capability as Cathode Material for Li-Ion Battery. **31,** 1527–1534 (2015).

72.   Zhang, X. *et al.* Facile polymer-assisted synthesis of LiNi0.5Mn1.5O4 with a hierarchical micro–nano structure and high rate capability. *RSC Adv.* **2,** 5669 (2012).

73.   Zheng, Z. *et al.* Host Structural Stabilization of Li1.232Mn0.615Ni0.154O2 through K-Doping Attempt: toward Superior Electrochemical Performances. *Electrochim. Acta* **188,** 336–343 (2016).

74.   Du, K., Zhang, L.-H., Cao, Y.-B., Peng, Z.-D. & Hu, G.-R. Synthesis of LiMn0.8Fe0.2PO4/C by co-precipitation method and its electrochemical performances as a cathode material for lithium-ion batteries. *Mater. Chem. Phys.* **136,** 925–929 (2012).

75.   Zhao, R., Chen, Z., Zhang, Y., Du, P. & Chen, H. *Ultrasonic/microwave-assisted co-precipitation method in the synthesis of Li1.1Mn0.433Ni0.233Co0.233O2 cathode material for lithium-ion batteries. Materials Letters* **136,** (2014).

76.   Li, L. *et al.* Synthesis and electrochemical performance of cathode material Li1.2Co0.13Ni0.13Mn0.54O2 from spent lithium-ion batteries. *J. Power Sources* **249,** 28–34 (2014).

77.   Nan, J., Han, D., Cui, M., Yang, M. & Pan, L. Recycling spent zinc manganese dioxide batteries through synthesizing Zn–Mn ferrite magnetic materials. *J. Hazard. Mater.* **133,** 257–261 (2006).

78.   Wang, D., Belharouak, I., Zhou, G. & Amine, K. Synthesis of Lithium and Manganese-Rich Cathode Materials via an Oxalate Co-Precipitation Method. *J. Electrochem. Soc.* **160,**

A3108–A3112 (2013).

79. Yang, Z. *et al.* Stepwise co-precipitation to synthesize LiNi1/3Co1/3Mn1/3O2 one-
     dimensional hierarchical structure for lithium ion batteries. *J. Power Sources* **272,** 144–
     151 (2014).

80. Liu, H. *et al.* Controllable synthesis of spinel lithium nickel manganese oxide cathode
     material with enhanced electrochemical performances through a modified oxalate co-
     precipitation method. *J. Power Sources* **274,** 1180–1187 (2015).

81. Van Bomme, A. & Dahn, J. R. Analysis of the growth mechanism of coprecipitated
     spherical and dense nickel, manganese, and cobalt-containing hydroxides in the presence
     of aqueous ammonia. *Chem. Mater.* **21,** 1500–1503 (2009).

82. Mielniczek-Brzóska, E. The nature of Mn(II) complexes in concentrated aqueous
     ammonium oxalate solutions. *Cryst. Res. Technol.* **45,** 1295–1304 (2010).

83. Watters, J. I. & DeWitt, R. The Complexes of Nickel(II) Ion in Aqueous Solutions
     Containing Oxalate Ion and Ethylenediamine1. *J. Am. Chem. Soc.* **82,** 1333–1339 (1960).

84. Groult, H., Nakajima, T. & Kumagai, N. Characterization and electrochemical properties
     of. **62,** 107–112 (1996).

85. Wang, D., Belharouak, I., Koenig, G. M., Zhou, G. & Amine, K. Growth mechanism of
     Ni0.3Mn0.7CO3 precursor for high capacity Li-ion battery cathodes. *J. Mater. Chem.* **21,**
     9290 (2011).

86. Noh, M. & Cho, J. Optimized Synthetic Conditions of LiNi0.5Co0.2Mn0.3O2 Cathode
     Materials for High Rate Lithium Batteries via Co-Precipitation Method. *J. Electrochem.*

Soc. **160,** A105–A111 (2013).

87.   Du, K. *et al.* Synthesis of LiFe0.4Mn0.6−x Ni x PO4/C by co-precipitation method and its electrochemical performances. *J. Appl. Electrochem.* **41,** 1349 (2011).

88.   Fan, J. *et al.* Hydrothermal-Assisted Synthesis of Li-Rich Layered Oxide Microspheres with High Capacity and Superior Rate-capability as a Cathode for Lithium-ion Batteries. *Electrochim. Acta* **173,** 7–16 (2015).

89.   Ren, W., Zhao, Y., Hu, X. & Xia, M. Preparation-microstructure-performance relationship of Li-rich transition metal oxides microspheres as cathode materials for lithium ion batteries. *Electrochim. Acta* **191,** 491–499 (2016).

90.   Li, L. *et al.* Ultrasonic-assisted co-precipitation to synthesize lithium-rich cathode Li1.3Ni0.21Mn0.64O2+d materials for lithium-ion batteries. *J. Power Sources* **272,** 922–928 (2014).

91.   Bai, Y. *et al.* Lithium-Rich Nanoscale Li1.2Mn0.54Ni0.13Co0.13O2 Cathode Material Prepared by Co-Precipitation Combined Freeze Drying (CP–FD) for Lithium-Ion Batteries. *Energy Technol.* **3,** 843–850 (2015).

92.   Wang, H. *et al.* Large-Scale Synthesis of NaNi1/3Fe1/3Mn1/3O2 as High Performance Cathode Materials for Sodium Ion Batteries. *J. Electrochem. Soc.* **163,** A565–A570 (2016).

93.   Li, J. *et al.* Synthesis, characterization and electrochemical performance of high-density aluminum substituted α-nickel hydroxide cathode material for nickel-based rechargeable batteries. *J. Power Sources* **270,** 121–130 (2014).

94.   Ju, J.-H. & Ryu, K.-S. Synthesis and electrochemical performance of Li(Ni0.8Co0.15Al0.05)0.8(Ni0.5Mn0.5)0.2O2 with core–shell structure as cathode material for Li-ion batteries. *J. Alloys Compd.* **509,** 7985–7992 (2011).

95.   Xie, H., Hu, G., Du, K., Peng, Z. & Cao, Y. An improved continuous co-precipitation method to synthesize LiNi0.80Co0.15Al0.05O2 cathode material. *Journal of Alloys and Compounds* **666,** 84–87 (2016).

96.   Koenig, G. M., Belharouak, I., Deng, H., Sun, Y.-K. & Amine, K. Composition-Tailored Synthesis of Gradient Transition Metal Precursor Particles for Lithium-Ion Battery Cathode Materials. *Chem. Mater.* **23,** 1954–1963 (2011).

97.   Koenig, G. M., Belharouak, I., Wu, H. M. & Amine, K. Hollow lithiated metal oxide particles as lithium-ion battery cathode materials. *Electrochim. Acta* **56,** 1426–1431 (2011).

98.   Fan, J. *et al.* Hydrothermal-Assisted Synthesis of Li-Rich Layered Oxide Microspheres with High Capacity and Superior Rate-capability as a Cathode for Lithium-ion Batteries. *Electrochim. Acta* **173,** 7–16 (2015).

99.   Zheng, Z., Guo, X., Chou, S., Hua, W. & Liu, H. Electrochimica Acta Designed Synthesis and Their Improved Electrochemical Performance. *Electrochim. Acta* **191,** 401–410 (2016).

100.   Zhang, S., Deng, C., Fu, B. L., Yang, S. Y. & Ma, L. Synthetic optimization of spherical Li[Ni1/3Mn1/3Co1/3]O2 prepared by a carbonate co-precipitation method. *Powder Technol.* **198,** 373–380 (2010).

101. Liu, G. B., Liu, H. & Shi, Y. F. Electrochimica Acta The synthesis and electrochemical properties of x Li 2 MnO 3 –(1 − x) MO 2 (M = Mn 1 / 3 Ni 1 / 3 Fe 1 / 3) via co-precipitation method. *Electrochim. Acta* **88,** 112–116 (2013).

102. Li, L. *et al.* Ultrasonic-assisted co-precipitation to synthesize lithium-rich cathode Li1.3Ni0.21Mn0.64O2+d materials for lithium-ion batteries. *J. Power Sources* **272,** 922–928 (2014).

103. Zhong, G. B., Wang, Y. Y., Yu, Y. Q. & Chen, C. H. Electrochemical investigations of the LiNi0.45M0.10Mn1.45O4 (M=Fe, Co, Cr) 5V cathode materials for lithium ion batteries. *J. Power Sources* **205,** 385–393 (2012).

104. Zhang, M., Wang, J., Xia, Y. & Liu, Z. Microwave synthesis of spherical spinel LiNi0.5Mn1.5O4 as cathode material for lithium-ion batteries. *J. Alloys Compd.* **518,** 68–73 (2012).

105. Jin, Y.-C. & Duh, J.-G. Nanostructured LiNi0.5Mn1.5O4 cathode material synthesized by polymer-assisted co-precipitation method with improved rate capability. *Mater. Lett.* **93,** 77–80 (2013).

106. Hwang, B. J., Wu, Y. W., Venkateswarlu, M., Cheng, M. Y. & Santhanam, R. Influence of synthesis conditions on electrochemical properties of high-voltage Li1.02Ni0.5Mn1.5O4 spinel cathode material. *J. Power Sources* **193,** 828–833 (2009).

107. Xia, H., Tang, S. B., Lu, L., Meng, Y. S. & Ceder, G. The influence of preparation conditions on electrochemical properties of LiNi0.5Mn1.5O4 thin film electrodes by PLD. *Electrochim. Acta* **52,** 2822–2828 (2007).

108. Aurbach, D. *et al.* Studies of cycling behavior, ageing, and interfacial reactions of LiNi0.5Mn1.5O4 and carbon electrodes for lithium-ion 5-V cells. *J. Power Sources* **162,** 780–789 (2006).

109. Amdouni, N., Zaghib, K., Gendron, F., Mauger, a. & Julien, C. M. Magnetic properties of LiNi0.5Mn1.5O4 spinels prepared by wet chemical methods. *J. Magn. Magn. Mater.* **309,** 100–105 (2007).

110. Santhanam, R. & Rambabu, B. Research progress in high voltage spinel LiNi0.5Mn1.5O4 material. *J. Power Sources* **195,** 5442–5451 (2010).

111. Risthaus, T. *et al.* Synthesis of spinel LiNi0.5Mn1.5O4 with secondary plate morphology as cathode material for lithium ion batteries. *J. Power Sources* **293,** 137–142 (2015).

112. Hong, S.-K., Mho, S.-I., Yeo, I.-H., Kang, Y. & Kim, D.-W. Structural and electrochemical characteristics of morphology-controlled Li[Ni0.5Mn1.5]O4 cathodes. *Electrochim. Acta* **156,** 29–37 (2015).

113. Kunduraci, M. *et al.* High-Power Nanostructured LiMn2-xNixO4 High-Voltage Lithium-Ion Battery Electrode Materials: *Chem. Mater* **18,** 3585–3592 (2006).

114. Chemelewski, K. R., Shin, D. W., Li, W. & Manthiram, A. Octahedral and truncated high-voltage spinel cathodes: the role of morphology and surface planes in electrochemical properties. *J. Mater. Chem. A* **1,** 3347 (2013).

115. Qian, Y. *et al.* Investigation of the Effect of Extra Lithium Addition and Postannealing on the Electrochemical Performance of High-Voltage Spinel LiNi0.5Mn1.5O4 Cathode Material. *J. Phys. Chem. C* **118,** 15581–15589 (2014).

116. Lin, H. B. *et al.* Crystallographic facet- and size-controllable synthesis of spinel LiNi0.5Mn1.5O4 with excellent cyclic stability as cathode of high voltage lithium ion battery. *J. Mater. Chem. A* **2,** 11987–11995 (2014).

117. Cho, H.-M., Chen, M. V., MacRae, A. C. & Meng, Y. S. Effect of Surface Modification on Nano-Structured LiNi $_{0.5}$ Mn $_{1.5}$ O $_4$ Spinel Materials. *ACS Appl. Mater. Interfaces* 150724153448006 (2015). doi:10.1021/acsami.5b01392

118. Song, J. *et al.* Role of Oxygen Vacancies on the Performance of Li[Ni 0.5 −. **4,** (2012).

119. Kim, J.-H., Myung, S.-T., Yoon, C. S., Kang, S. G. & Sun, Y.-K. Comparative Study of LiNi0.5Mn1.5O4-δ and LiNi0.5Mn1.5O4 Cathodes Having Two Crystallographic Structures: Fd ̄3m and P 4332. *Chem. Mater.* **16,** 906–914 (2004).

120. Wu, W. W. *et al.* Ordered LiNi0.5Mn1.5O4 hollow microspheres as high-rate 5V cathode materials for lithium ion batteries. *Electrochim. Acta* **119,** 206–213 (2014).

121. Xiao, J. *et al.* High-performance LiNi 0.5Mn 1.5O 4 Spinel controlled by Mn 3+ concentration and site disorder. *Adv. Mater.* **24,** 2109–2116 (2012).

122. Wan, L. *et al.* Ni/Mn ratio and morphology-dependent crystallographic facet structure and electrochemical properties of the high-voltage spinel LiNi\n 0.5\n Mn\n 1.5\n O\n 4\n cathode material. *RSC Adv.* **5,** 25988–25997 (2015).

123. Thackeray, M. M. Lithiated Oxides for Lithium Ion Batteries. *J. Electrochem. Soc.* **142,** 2558–2563 (1995).

124. Dokko, K., Mohamedi, M., Anzue, N., Itoh, T. & Uchida, I. In situ Raman spectroscopic studies of LiNixMn2-xO4 thin film cathode materials for lithium ion secondary batteries.

J. Mater. Chem. **12,** 3688–3693 (2002).

125. Wang, D. *et al.* Synthesis of high capacity cathodes for lithium-ion batteries by morphology-tailored hydroxide co-precipitation. *J. Power Sources* **274,** 451–457 (2015).

126. Nam, K.-M., Kim, H.-J., Kang, D.-H., Kim, Y.-S. & Song, S.-W. Ammonia-free coprecipitation synthesis of a Ni-Co-Mn hydroxide precursor for high-performance battery cathode materials. *Green Chem.* **17,** 1127–1135 (2015).

127. Yang, Y. *et al.* Growth mechanisms for spherical mixed hydroxide agglomerates prepared by co-precipitation method: A case of Ni1/3Co1/3Mn1/3(OH)2. *J. Alloys Compd.* **619,** 846–853 (2015).

128. Xiang, Y., Yin, Z. & Li, X. An improved carbonate precipitation method for the preparation of Li1.2Ni0.12Co0.12Mn0.56O2 cathode material. *Ionics (Kiel).* **20,** 163–168 (2014).

129. Zhu, X. *et al.* Porous LiNi0.5Mn1.5O4 microspheres with different pore conditions: Preparation and application as cathode materials for lithium-ion batteries. *J. Power Sources* **261,** 93–100 (2014).

130. Prabaharan, S. R. S. *et al.* Bulk synthesis of submicrometre powders of LiMn2O4 for secondary lithium batteries. *J. Mater. Chem.* **5,** 1035–1037 (1995).

131. Gao, X. & Dollimore, D. The thermal decomposition of oxalates. *Thermochim. Acta* **215,** 47–63 (1993).

132. Guillemet-Fritsch, S. *et al.* High-quality nickel manganese oxalate powders synthesized in a new segmented flow tubular reactor. *Solid State Ionics* **171,** 135–140 (2004).

Appendix

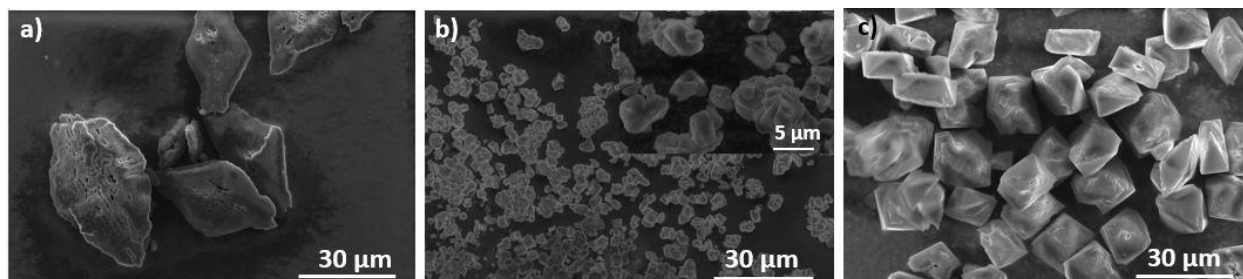**SEM Images of Precursors and LNMO.**

Figure A 1. SEM images of a) pure manganese oxalate particles, b) pure nickel oxalate particles, and c) Mn/Ni 3/1 oxalate particles. All particles are collected from 20mM batch.
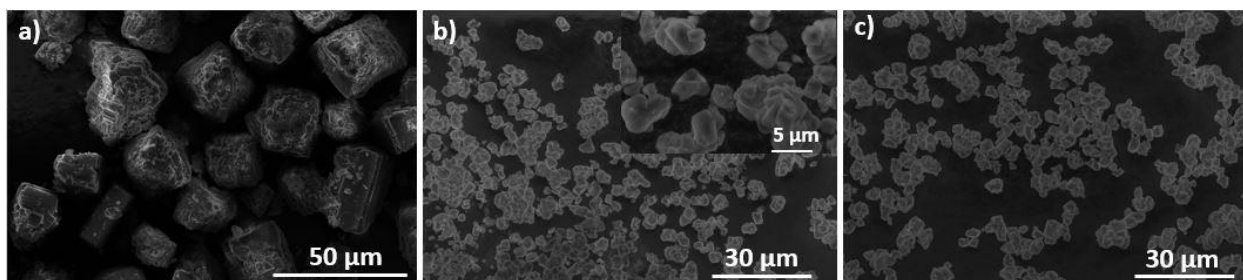

Figure A 2. SEM images of a) manganese oxalate seeds, b) pure nickel particles, and c) nickel particles collected from seeding batch. The seeds were collected from pure manganese oxalate batch of 100mM and the particles were collected right after mixing.
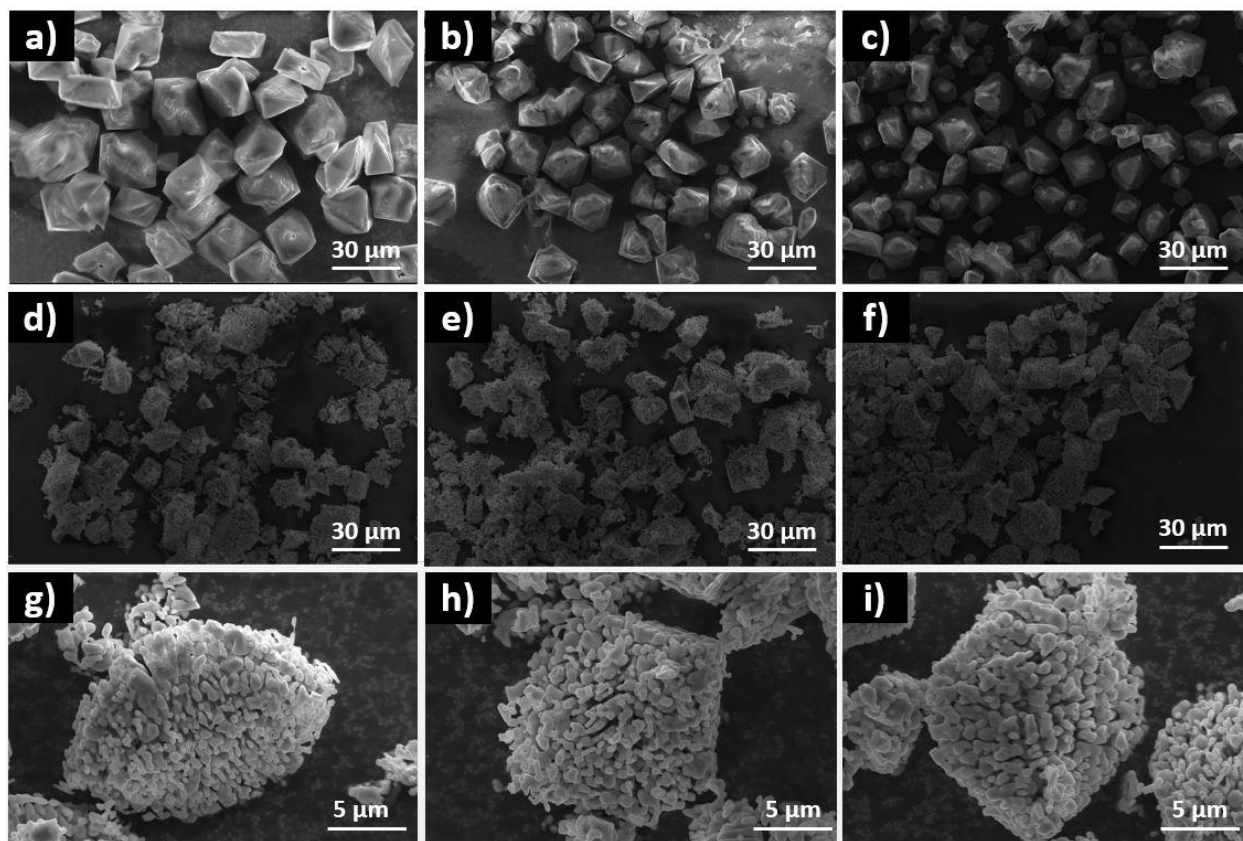
Figure A 3. SEM images of a) manganese rich, b) stoichiometric, and c) nickel rich precursors, and their corresponding LNMOs.
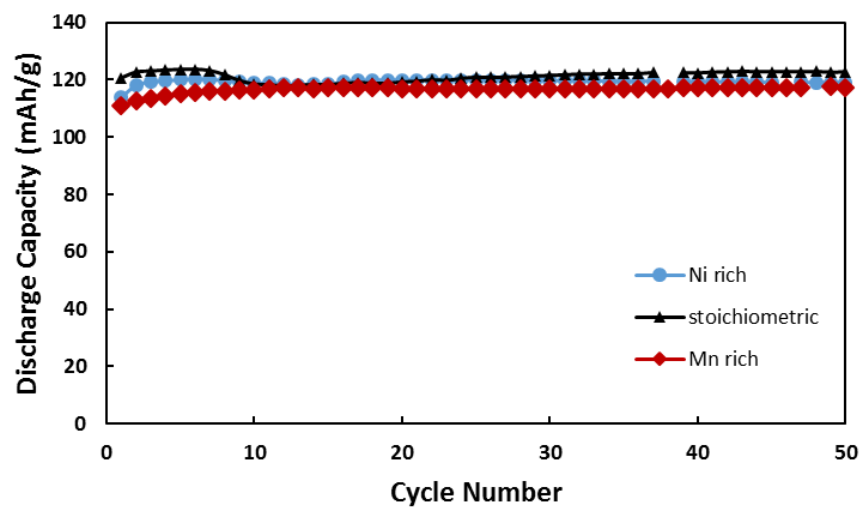
Cycle Performance Tests

Figure A 4. Cycling performance tests of manganese rich, stoichiometric, and nickel rich LNMO cells. Each cycle is charged and discharged at C/10 rate.

Tables.

Table A 1. The Mn/Ni ratios from equilibrium calculation and ICP measurement under different concentrations.

Feed Concentration (mol/L)	Equilibrium Calculation	Measured using ICP	Deviation (%)
0.10	2.88	2.97	3.28
0.05	2.76	2.68	3.64
0.02	2.38	2.60	13.7
0.01	1.72	2.18	35.6